Radar Autofocus Algorithm Incorporating *a priori* Terrain Knowledge for Correction of Mars' Ionospheric Distortion in MARSIS Observations

Joseph G. McMichael, Yonggyu Gim, Darmindra D. Arumugam, Jeffrey J. Plaut
NASA Jet Propulsion Laboratory
California Institute of Technology
4800 Oak Grove Drive, Pasadena, CA 91109
Emails: {joseph.g.mcmichael, yonggyu.gim, darmindra.d.arumugam, jeffrey.j.plaut}@jpl.nasa.gov

***Abstract*—Low-frequency subsurface radar observations of Mars' polar ice deposits by MARSIS (Mars Advanced Radar for Subsurface and Ionosphere Sounding) are heavily impacted by the electron content of Mars' ionosphere. The resulting ionospheric distortion can be represented as attenuation and bulk delay, in addition to higher-order frequency dispersion effects. Baseline, uncorrected images are often unusable when the solar zenith angle is less than 90° (day side). In this work, a radar autofocus algorithm is developed that estimates and inverts ionospheric distortion, producing a focused radargram of the ice deposit subsurface. Previously published autofocus algorithms have sought to maximize peak-to-noise contrast, which may yield sub-optimal results for complex terrain. Instead, a maximum likelihood approach is developed that incorporates simulated surface clutter returns for the current spacecraft position, based on the Mars Orbiter Laser Altimeter (MOLA) elevation model of the Martian surface. An ancillary product is a surface-only clutter simulation for each orbit, which is necessary to identify true subsurface features.**

I. Introduction

Radar sounding instruments employ long-wavelength RF transmissions to penetrate ice deposits and reveal ice thickness, as well as internal layering. The MARSIS instrument (Mars Advanced Radar for Subsurface and Ionosphere Sounding) aboard Mars Express has been collecting data since 2005, accumulating over 7,200 radargrams in 16,000 orbits. The radar has the capability to simultaneously operate in two of four frequency bands centered at (1.8, 3, 4, 5 MHz), each with a 1 MHz bandwidth chirp. [1],[2] The resultant free-space depth resolution is 150 m, or approximately 85 m in the icy medium (assuming dielectric constant $\epsilon = 3.1$). In typical operation, the on-board processor synthesizes three beams in the along-track direction (reverse, nadir, forward) through unfocused Doppler processing of a synthetic aperture. Telemetry available for ground processing includes the Fourier-transformed azimuth beams, receiver trigger and automatic gain control settings, and the spacecraft location relative to IAU2000 Mars ellipse.

The dominant source of distortion in the return radar signal can be attributed to Mars' ionosphere. Wavefronts traversing the ionosphere experience attenuation, bulk delay, and higher-order frequency dispersion. The severity of the effect is dependent on the electron density profile beneath the spacecraft, and is considerably worse when the solar zenith angle is less than 90° (day side). The peak of the electron density profile is located at an altitude of 130-150 km. [3] A smaller, related source of distortion is Mars' crustal magnetic field, which interacts in a similar way with the propagating wavefront.

The electron density profile for an idealized ionosphere can be described with the Chapman model, developed in 1931. [3] A prediction of the current electron density can be made based on the current solar zenith angle. A simple, open-loop focusing approach is to attempt to focus a radargram by inverting the Chapman-predicted electron density profile. While this is adequate in some circumstances, the open-loop prediction often contains significant errors due to localized deviations from the idealized Chapman model.

Another common focusing approach is to apply a closed-loop optimization to maximize the peak-to-noise contrast ratio of the radargram. In effect, the total electron content (TEC) is estimated that maximizes the peak value of the radargram. This approach assumes that the surface will produce a strong, specular response, which is then blurred by the ionosphere. However, the technique may add artifacts if the Martian terrain within the beam is complex, containing plateaus or multiple crater beds. In these cases, the true range profile should actually contain multiple strong reflections at different heights, rather than a single reflection. It is likely that simply maximizing peak-to-noise ratio will "merge" distinct peaks to produce an artifically large single reflecting surface.

In this work, we develop an alternative maximum likelihood focusing algorithm that incorporates *a priori* knowledge of the Martian terrain. The Mars Orbiter Laser Altimeter (MOLA) provides precise elevation measurements at approximately 500 m spacing over the entire Martian surface, with better resolution near the poles. The optimization we have devised consists of maximizing correlation with a simulated MOLA-derived return depth profile based on the current spacecraft location and antenna aspect angle. For simple, flat terrain this reduces to peak-to-noise contrast maximization, as we are effectively correlating against an delta function. However, in cases when multiple surface reflections are present from different heights (e.g. plateau with surrounding lowlands), this approach does not artificially constrain the return to have a single large peak. Instead, multi-peak returns can be accurately focused by comparing their correlation with the MOLA-derived clutter simulation profile.

The research was carried out at the Jet Propulsion Laboratory, California Institute of Technology, under a contract with the National Aeronautics and Space Administration. Copyright 2016 California Institute of Technology. U.S. Government sponsorship acknowledged.

II. Ionospheric Signal Distortion Model

The effect of signal propagation through Mars' ionosphere can be modeled as a linear combination of phase basis functions in the frequency domain. [3] For a given electron density profile $N_e(z)$ describing the vertical column beneath the spacecraft as a function of altitude z, the phase shift $\phi(f)$ can be expressed as:

$$\phi(f) = \frac{-2\pi}{c}\left(\frac{8.98^2}{f}\underbrace{\int N_e(z)dz}_{TEC,\Psi_1} + \frac{8.98^4}{3f^3}\underbrace{\int N_e^2(z)dz}_{TEC,\Psi_2} + \frac{8.98^6}{8f^5}\underbrace{\int N_e^3(z)dz}_{TEC,\Psi_3}\right), \quad (1)$$

where f is the frequency in units of MHz and c is the speed of light. The three basis functions $\Psi_{1,2,3}$ are proportional to $1/f$, $1/f^3$, and $1/f^5$, respectively. These are illustrated in Fig. 1 for the band 4.5-5.5 MHz, with dashed lines showing linear fits to the basis functions.

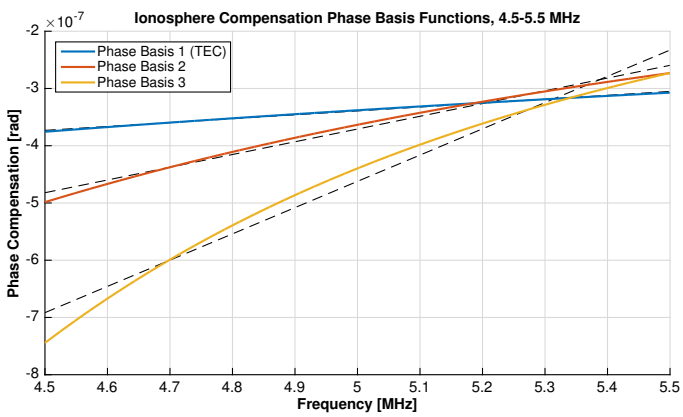

Fig. 1. Ionospheric model phase basis functions in the frequency domain, for the band 4.5-5.5 MHz. Dashed lines represent linear fits for each curve. The slope of the linear component of each basis function is equivalent to bulk delay, while the residual curvature causes additional dispersion.

The slope of the linear component of each basis function is particularly important, as this determines the pure delay associated with each Ψ coefficient. This relationship can be seen by considering the Fourier transform pair in eq. 2, in which a linear phase ramp with slope $-t_0$ (in angular frequency ω), or $-2\pi t_0$ (in frequency f) corresponds to a pure delay t_0, and $\mathcal{F}$ denotes the Fourier transform.

$$\mathcal{F}\{x(t-t_0)\} \rightarrow \mathrm{e}^{-j\omega t_0}\mathrm{X}(j\omega) \quad (2)$$

Thus, each ionospheric coefficient Ψ provides its own effective delay, independent of the other two parameters. The total effective delay is the sum of all three components. It is straightforward to estimate the associated delay of each basis function in "samples per unit" for each band. The effective ADC sample rate after conversion to complex I/Q is 1.4 MHz, so the sample period corresponds to 0.7143 μs.

	Ψ_1 Delay (samp/unit)	Ψ_2 Delay (samp/unit)	Ψ_3 Delay (samp/unit)
Band 1 (1.8 MHz)	8.71e-8	2.43e-6	4.50e-5
Band 2 (3 MHz)	3.04e-8	2.83e-7	1.69e-6
Band 3 (4 MHz)	1.70e-8	8.75e-8	2.85e-7
Band 4 (5 MHz)	1.08e-8	3.54e-8	7.30e-8

TABLE I. Table of pure delay component in each band for three ionosphere coefficients. Results are displayed in "samples/unit," where processing is done at the complex I/Q sample rate of 1.4 MHz, or 0.7143 μs per sample.

This table of pure delay components is constant, and may be precomputed prior to focusing. As will be described in the next section, a key insight to improve the efficiency of the optimization algorithm is to "prune" solutions with unrealistic summed delays. Immediately eliminating unfeasible solutions dramatically improves the run-time performance of the algorithm. Note that while the pruning is done based on effective pure delay, the actual phase compensation applied includes the full curvature of the phase basis functions (not just the linear component).

III. Baseline Processing

Telemetry from the spacecraft includes Fourier-transformed I/Q data, denoted $X(\omega)$ here, for each beam after unfocused Doppler processing has been applied by the on-board processor. However, pulse compression with the transmitted chirp has not yet been applied. Also, the receiver trigger delay varies over the course of an orbit, and must be compensated for. Standard ground processing is done in the frequency domain to get the pulse-compressed baseline output $Y(\omega)$:

$$Y(\omega) = \mathcal{F}\big[\text{ZERO-PAD } \mathcal{F}^{-1}\big[X(\omega)\big]\big] \cdot \mathcal{F}\big[\text{ZERO-PAD } \mathcal{F}^{-1}\big[C^*(\omega)\big]\big] \cdot \mathrm{e}^{-j\omega t_{trig}}, \quad (3)$$

where $C^*(\omega)$ is the conjugated frequency response of the chirp transmission, and t_{trig} is the delay necessary to align the receiver windows across multiple pulses. Because Discrete Fourier Transforms (DFTs) are being utilized, zero-padding must be done to ensure that the convolution operation is linear and not circular. Finally, the spectrum $Y(\omega)$ is transformed to obtain the time-domain pulse-compressed baseline output, $y[n]$.

The uncompensated effects of the ionosphere tend to be quite severe. An example is shown in Fig. 2 for Orbit 8700. The expected nadir delay from MOLA at each spacecraft position is shown with a red trace. When the solar zenith angle is high (on the left side), the deviation is minor. However, for smaller solar zenith angle, the delay approaches 150 μs. The surface return is not only delayed, but it is also significantly blurred by dispersion. The lower portion of the figure shows the terrain for this particular orbit, as extracted from MOLA.

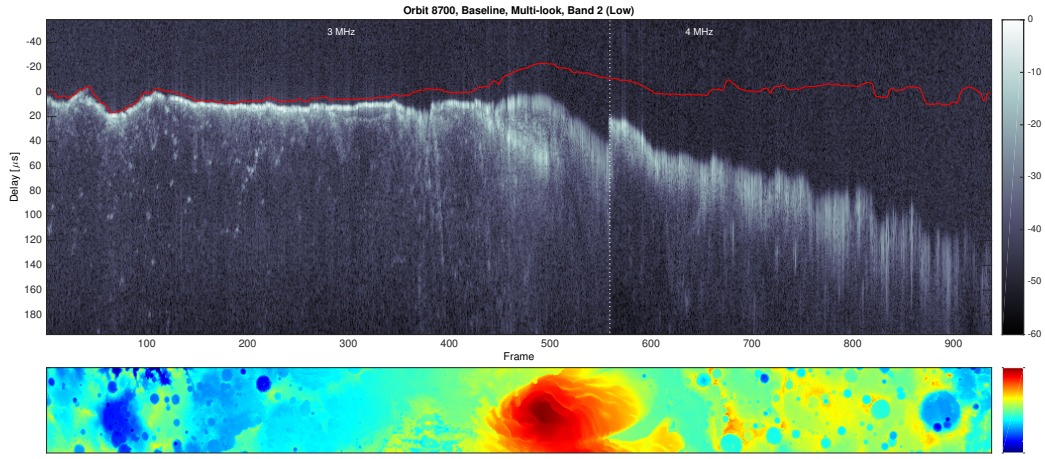

Fig. 2. Baseline radargram for orbit 8700, without correction for ionospheric effects. Radar return is delayed and blurred as the solar zenith angle decreases from left to right. The South Polar Layered Deposit (SPLD) is present in the center of the scene. Above: radargram with red trace showing expected nadir delay vs. along-track position. Below: MOLA digital elevation model for this orbit.

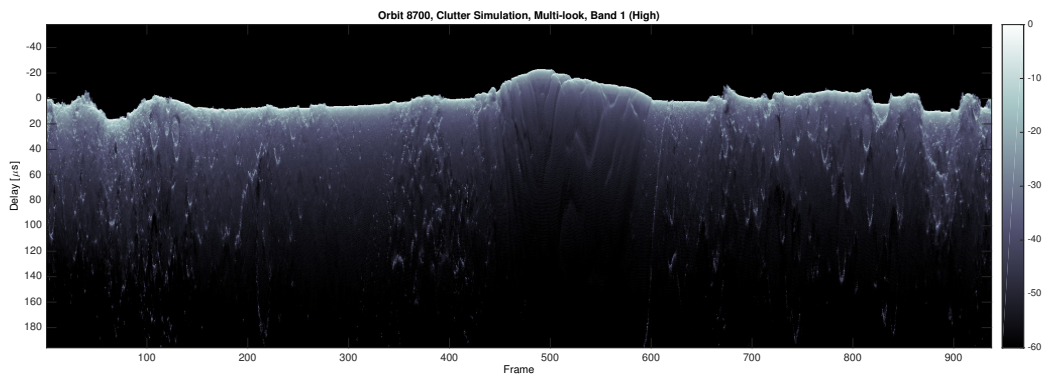

Fig. 3. MOLA-derived radar clutter simulation for orbit 8700, based on terrain within beam at current spacecraft position. Simulation includes any off-nadir surface features features that will "lay-over" into the beam. Sub-surface features will not show up in simulation. The Martian surface has been tessellated, and the radar look angle computed relative to the normal vector for each patch. Hagfors' Scattering Law was used to model specular and diffuse components of surface return.

IV. Clutter Simulation

A realistic simulation of the "clutter" signal from surface scatterers on- and off-nadir is necessary for the maximum likelihood algorithm introduced in the next section. We have developed software to simulate the expected radar response at a given spacecraft position from surface scattering facets, using the high-resolution MOLA digital elevation model of Martian terrain.

The MARSIS beampattern is quite wide in the cross-track direction (400 km cross-track, 25 km along-track). Thus, it is often the case that off-nadir scatterers will arrive at the same delay as true sub-surface reflections. Disambiguating these requires a simulation of the expected return from surface scatterers. Any reflection present in the radargram and not in the clutter simulation is likely from a true subsurface object.

The following steps are taken to create a clutter simulation. For each spacecraft XYZ position in the orbit:

1) Extract MOLA points within current beam footprint (25 km along-track x 400 km cross-track)
2) Compute Euclidean range to each point
3) Use Hagfors' Scattering Law to compute expected $RCS(\phi_{inc})$ for each facet
   - Calculate normal vector of each facet of DEM (based on terrain slope)
   - Compute incidence angle to each facet, ϕ_{inc}
4) Apply synthetic beam pattern (8 km along-track) and combine non-coherently

The Hagfors' Scattering Law was developed by Tor Hagfors to model scattering of planetary surfaces, with a specular and diffuse component. [4] The opposite-sense circular return can be expressed as:

$$\sigma_0(\phi_{inc}) = \frac{C\rho_0}{2}\left[\cos^4\phi_{inc} + C\sin^2\phi_{inc}\right]^{-3/2} + A\cos^n\phi_{inc}, \tag{4}$$

where C, ρ_0, A, and n are parameters that describe the roughness of the surface, and proportion of coherent to diffuse returns. An example clutter simulation is displayed in Fig. 3 for orbit 8700. We have found that many features of the actual radargrams match up well with the simulated versions.

This will become important in the next section, where the simulations are employed as *a priori* knowledge to improve focusing.

V. Autofocus Metric

In order to compensate for ionospheric distortion, the electron density profile must be estimated and its affects inverted. If the time-varying parameters of the ionosphere are perfectly known, this simply involves adding a multiplicative term to the baseline processing chain in eq. 3, from the compensation expression in eq. 1.

$$\begin{aligned} Y(\omega) = \mathcal{F}\big[&\text{ZERO-PAD } \mathcal{F}^{-1}\big[X(\omega)\big]\big] \\ &\cdot \mathcal{F}\big[\text{ZERO-PAD } \mathcal{F}^{-1}\big[C^*(\omega)\big]\big] \cdot \mathrm{e}^{-j\omega t_{trig}} \\ &\cdot \exp\left\{\frac{-j2\pi}{c}\left(\frac{8.98^2\Psi_1}{f} + \frac{8.98^4\Psi_2}{3f^3} + \frac{8.98^6\Psi_3}{8f^5}\right)\right\} \end{aligned} \quad (5)$$

However, this type of open-loop correction rarely performs well in low solar zenith angle conditions on the day-side of the planet. Instead, a closed-loop optimization is required to maximize performance. Most current closed-loop autofocus algorithms rely on maximizing peak-to-noise contrast. This works well for smooth terrain with a single dominant reflection, but often adds artifacts when several scatterers are present at different heights (e.g. a plateau with surrounding lowlands). Focusing to a single elevation does not capture the subtlety of off-nadir "layover" near the surface.

In this work, an alternative focus metric is implemented which maximizes correlation with an *a priori* clutter simulation. For a given orbit radargram $r(\Psi)$ which has been compensated for ionospheric coefficients Ψ, and corresponding clutter simulation s, we are optimizing:

$$\Psi_{optim} = \underset{\Psi}{\operatorname{argmax}} \frac{\sum_n |r(\Psi,n)|^2 \cdot |s(\Psi,n)|^2}{\left|\sum_{n,\text{before MOLA}} r(\Psi,n)\right|^2} \quad (6)$$

where the depth sample index is denoted n. The numerator of eq. 6 captures the correlation of the compensated depth profile with the expected clutter simulation, and the denominator is a penalty term that avoids focusing to sub-surface echoes. The penalty term involves integrating the total power of the compensated radargrams before the expected MOLA-derived nadir delay. Without this penalty, the correlation metric may occasionally erroneously align with subsurface ice interfaces.

Two examples from MARSIS orbit 15151 are displayed in Figs. 4 and 5. The first is for a smooth scene with no subsurface reflections present (single peak in measured depth profile). The focusing algorithm easily aligns the compensated radargram depth profile with the expected clutter simulation.

The second example is considerably more difficult to focus correctly, containing at least three significant subsurface reflection peaks from objects not present in the clutter simulation. Ideally, the algorithm should align the left-most peak in the compensated data profile with the single peak present in the clutter simulation. Indeed, the penalty function acts as intended and ensures focusing of the complex scene while avoiding alignment to subsurface peaks.

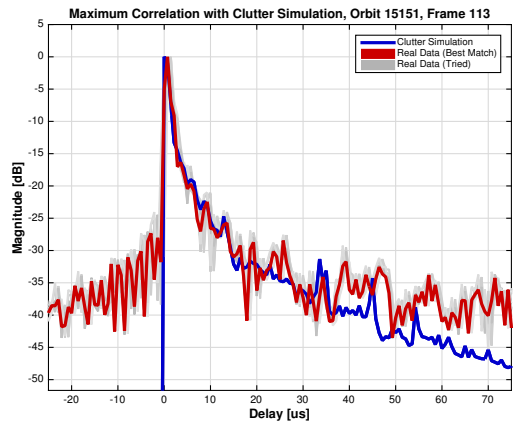

Fig. 4. Optimized radar depth profile for smooth scene (Orbit 15151, Frame 113), with no subsurface reflections present. The algorithm correctly aligns with the single expected peak from the clutter simulation. The red trace represents optimized depth profile. The blue and gray traces represent the clutter simulation depth profile and other ionosphere compensations applied, respectively.

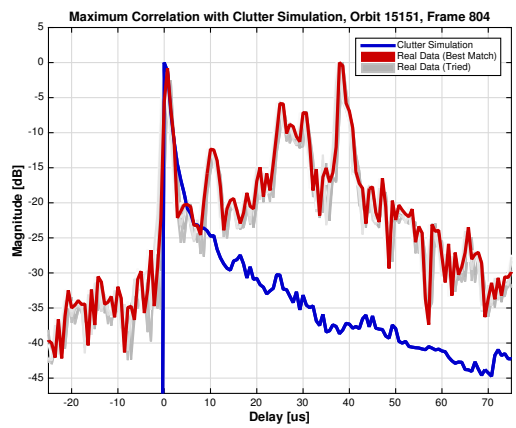

Fig. 5. Optimized radar depth profile for difficult scene (Orbit 15151, Frame 804), with several strong subsurface reflections present. The algorithm correctly aligns the earliest peak in the data to the peak from the clutter simulation. The red trace represents optimized depth profile. The blue and gray traces represent the clutter simulation depth profile and other ionosphere compensations applied, respectively.

VI. Feasible Solution Space

Performing the optimization in eq. 6 requires joint optimization over a 3-dimensional coefficient space. The problem is non-convex, so gradient descent approaches often converge to sub-optimal local maxima. Grid sampling at sufficient resolution over the entire 3-D space is generally not feasible for more than a few orbits.

One key insight is that the feasible solution space is much smaller than the full coefficient space. As discussed earlier, each coefficient Ψ has an associated pure time delay, independent of the other two. The approximate effective delay of the combined correction is equal to the summation of the three delays. This property can be exploited to immediately prune unfeasible solutions and significantly increase focusing

speed. This can be seen in the 2-D example in Fig. 6, where all of the feasible solutions lie along a distinct plane (within some tolerance).

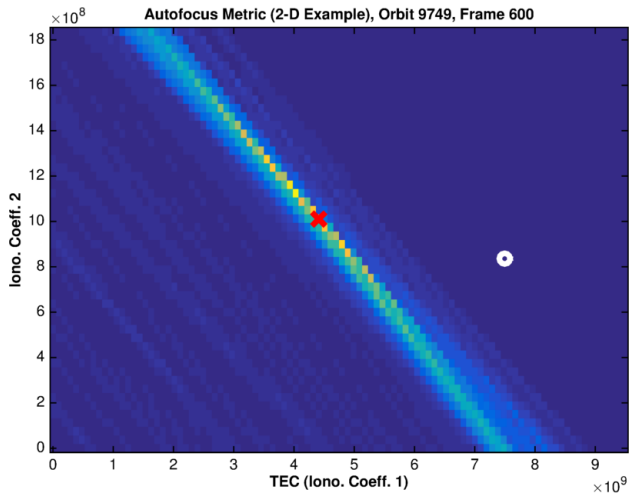

Fig. 6. Correlation metric swept over first two dimensions of ionospheric correction model Ψ_1 and Ψ_2 for Orbit 9749, Frame 600. Note that all feasible solutions lie along a plane (within some tolerance). Red 'x' denotes optimum and white circle denotes open-loop Chapman estimate. This illustrates the nature of the effective delays of the basis functions. The total sum of delays must match the expected MOLA delay to achieve a high-score. The smaller feasible subspace can be sampled to obtain solutions.

The algorithm progresses in the following order. First, to avoid sampling unfeasible solutions, the approximate delay between the expected MOLA nadir return and the distorted baseline is coarsely estimated. Although it is a coarse estimate, the approximate delay allows for elimination of solutions with combined effective delays outside of a tolerance window of ± 150 samples.

Next, a three-stage process is used to successively refine the overall ionosphere estimate Ψ_{optim}. At each stage, the tolerance window is tightened around the previous best estimate and higher sampling resolution is used. Finally, the best estimate Ψ_{optim} is used to compute the focused radargram. An experimental validation of the technique verified that 99.9% of solutions are identical to full grid search, with 140x speed improvement over the full grid search.

VII. Example Focused Radargrams

The focused result for orbit 8700 is shown in Figs. 7 and 9. After focusing, the South Polar Layered Deposit (SPLD) subsurface ice interface is clearly visible. Fig. 7 displays a close-up view of the focused SPLD, revealing internal layering within the ice sheets. In Fig. 9, a second thin subsurface interface between frames 300-360 is also now detectable. None of these features were visible in Fig. 2, which corresponds to the same radargram before focusing.

Fig. 8 displays estimated ionospheric coefficients $\Psi_{1,2,3}$ as a function of frame within orbit 8700. Note that Ψ_1 in particular significantly deviates from the open-loop Chapman estimate based on solar zenith angle alone.

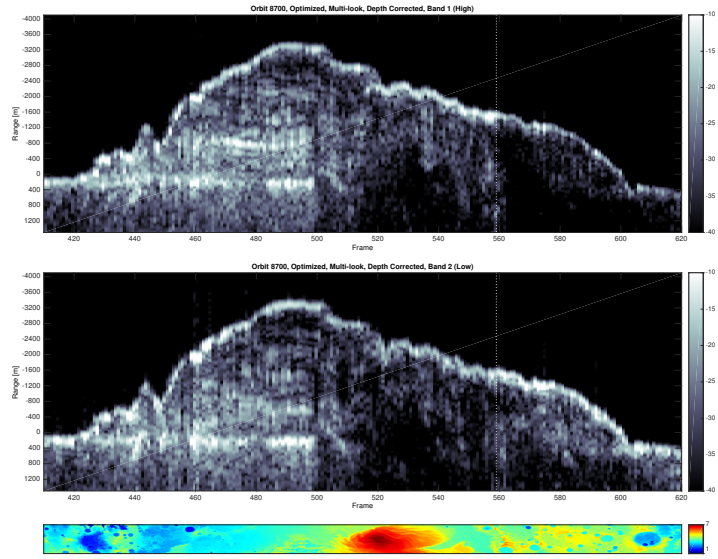

Fig. 7. Close-up view of focused radargram for orbit 8700, with South Polar Layered Deposit (SPLD) centered at frame 500. Top two subplots show different frequency band responses.

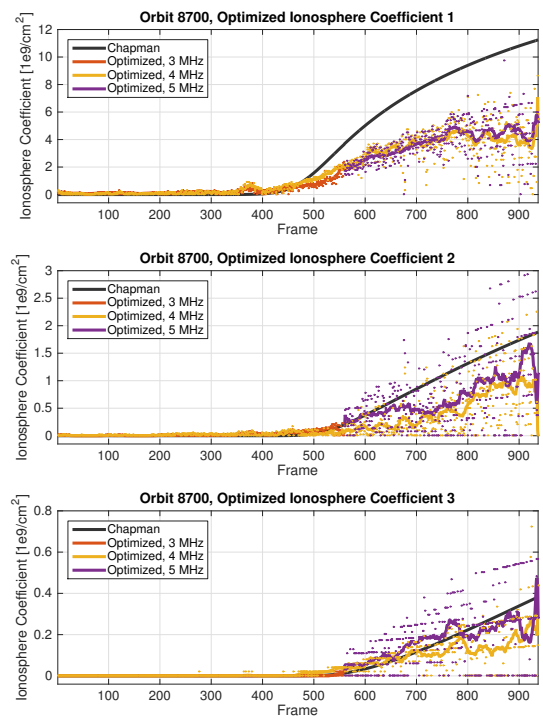

Fig. 8. Optimized ionospheric coefficients $\Psi_{1,2,3}$ as a function of frame within orbit 8700. Open-loop Chapman estimate is shown in black.

VIII. Conclusion

A radar autofocus algorithm has been developed that incorporates *a priori* knowledge of Martian terrain from MOLA. Rather than employing a maximum contrast metric, which may incorrectly add artifacts over complex terrain, this approach

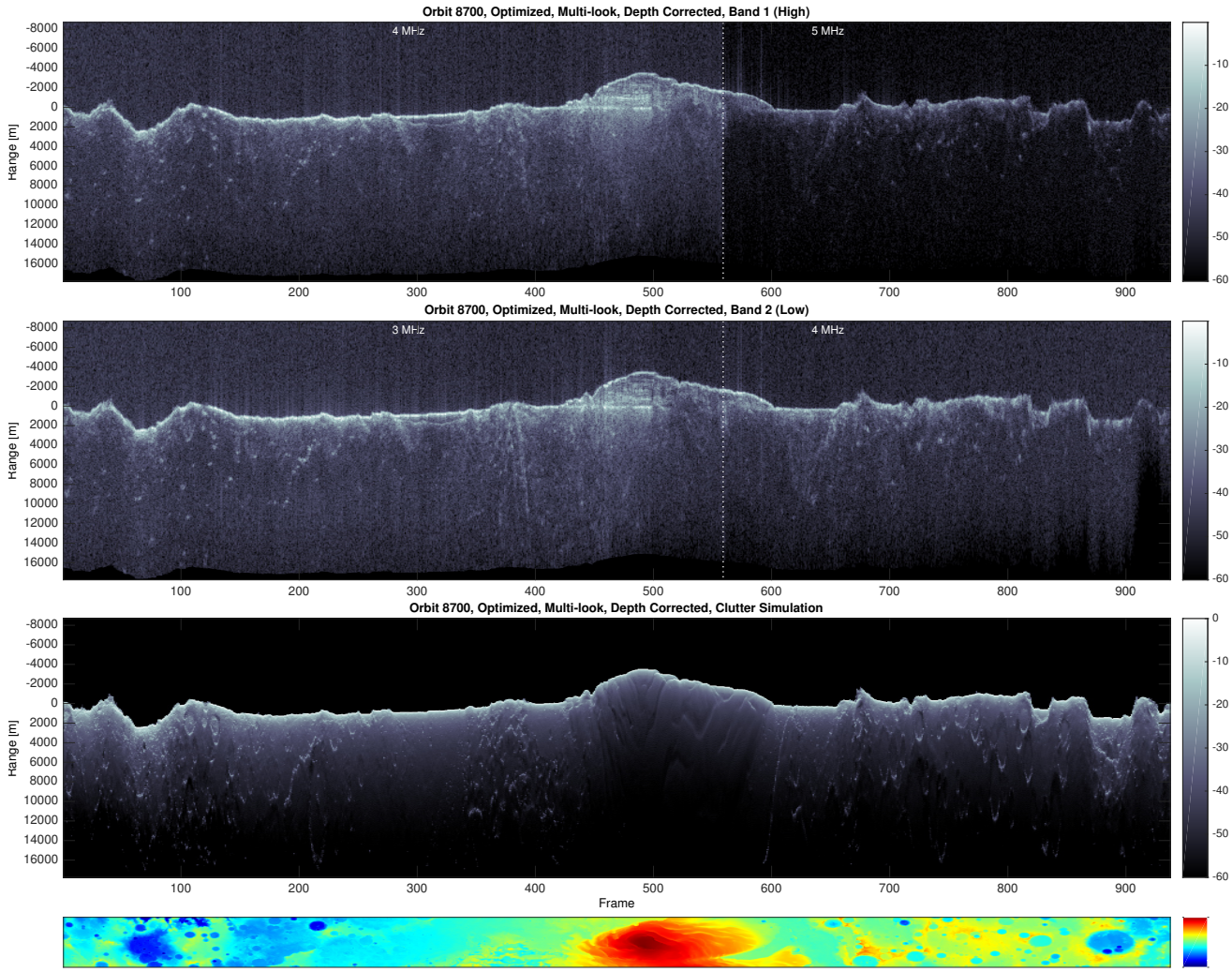

Fig. 9. Focused radargram for orbit 8700, with South Polar Layered Deposit (SPLD) centered at frame 500. The top two subplots show responses at different frequency bands. The bottom subplot displays the corresponding clutter simulation used in the process of focusing.

maximizes correlation with a clutter simulation. This approach results in well-focused radargrams over complex terrain that includes multiple scatterers at different heights. A penalty function has been described that avoids erroneous alignment of the compensated radargram to subsurface reflections not present in the clutter simulation. A key insight is that each phase basis function in the ionospheric distortion model has its own associated pure delay. This insight can be used to immediately "prune" unfeasible solutions and dramatically increase the speed of focusing. This technique has been implemented in multi-threaded C/C++ and employed to retroactively focus all 7,200 MARSIS radargrams recorded over 16,000 orbits to date.

References

[1] R. Orosei, et al., *Mars Advanced Radar for Subsurface and Ionospheric Sounding (MARSIS) after nine years of operation: A summary*, Planetary and Space Science, Volume 112, July 2015, Pages 98-114, ISSN 0032-0633, http://dx.doi.org/10.1016/j.pss.2014.07.010.

[2] R. Jordan, et al., *The Mars express MARSIS sounder instrument*, Planetary and Space Science, Volume 57, Issues 1415, December 2009, Pages 1975-1986, ISSN 0032-0633, http://dx.doi.org/10.1016/j.pss.2009.09.016.

[3] Safaeinili, A., et al., *Estimation of the total electron content of the Martian ionosphere using radar sounder surface echoes, Geophysical Research Letters*, 2007, 34, L23204, doi:10.1029/2007GL032154.

[4] Campbell, Bruce A. Radar remote sensing of planetary surfaces. Cambridge University Press, 2002.